Entropic evidence for a Pomeranchuk effect in magic-angle graphene

Entropic evidence for a Pomeranchuk effect in magic angle graphene

Asaf Rozen[1†], Jeong Min Park[2†], Uri Zondiner[1†], Yuan Cao[2†], Daniel Rodan-Legrain[2], Takashi Taniguchi[3], Kenji Watanabe[3], Yuval Oreg[1], Ady Stern[1], Erez Berg[1*], Pablo Jarillo-Herrero [2*] and Shahal Ilani[1*]

[1] *Department of Condensed Matter Physics, Weizmann Institute of Science, Rehovot 76100, Israel.*
[2] *Department of Physics, Massachusetts Institute of Technology, Cambridge, Massachusetts 02139, USA.*
[3] *National Institute for Materials Science, 1-1 Namiki, Tsukuba, 305-0044 Japan.*
[†] *These authors contributed equally to the work.*
[*]Correspondence to: erez.berg@weizmann.ac.il, pjarillo@mit.edu, shahal.ilani@weizmann.ac.il

In the 1950's, Pomeranchuk[1] predicted that, counterintuitively, liquid ^{3}He may solidify upon heating, due to a high excess spin entropy in the solid phase. Here, using both local and global electronic entropy and compressibility measurements, we show that an analogous effect occurs in magic angle twisted bilayer graphene. Near a filling of one electron per moiré unit cell, we observe a dramatic increase in the electronic entropy to about $1k_B$ per unit cell. This large excess entropy is quenched by an in-plane magnetic field, pointing to its magnetic origin. A sharp drop in the compressibility as a function of the electron density, associated with a reset of the Fermi level back to the vicinity of the Dirac point, marks a clear boundary between two phases. We map this jump as a function of electron density, temperature, and magnetic field. This reveals a phase diagram that is consistent with a Pomeranchuk-like temperature- and field-driven transition from a low-entropy electronic liquid to a high-entropy correlated state with nearly-free magnetic moments. The correlated state features an unusual combination of seemingly contradictory properties, some associated with itinerant electrons, such as the absence of a thermodynamic gap, metallicity, and a Dirac-like compressibility, and others associated with localized moments, such as a large entropy and its disappearance with magnetic field. Moreover, the energy scales characterizing these two sets of properties are very different: whereas the compressibility jump onsets at $T \sim 30\text{K}$, the bandwidth of magnetic excitations is $\sim 3\text{K}$ or smaller. The hybrid nature of the new correlated state and the large separation of energy scales have key implications for the physics of correlated states in twisted bilayer graphene.

1

Systems of strongly interacting fermions exhibit a competition between localization, minimizing the potential energy, and itineracy, minimizing the kinetic energy. The advent of two-dimensional moiré systems, such as magic angle twisted bilayer graphene[2–6] (MATBG), allows studying this physics by controlling the ratio between the electronic interactions and bandwidth in a highly tunable artificial lattice. In systems where this ratio is large, such as transition metal dichalcogenides hetero-bilayers, electrons tend to localize to the lattice sites, forming Mott insulators[7,8]. In the other extreme, where the electronic bandwidth is large, as in bilayer graphene with a large twist angle, a Fermi liquid state is formed in which electrons are itinerant. MATBG provides a fascinating example of a system at the boundary between these two extremes. This system shows a host of electronic phases, including correlated insulators[3,9,10], Chern insulators[11–13], superconductors[4,9,10], and ferromagnets[14,15]. Scanning tunneling spectroscopy[16–19] and electronic compressibility measurements[20,21] indicate that in this system the strengths of the Coulomb interaction and the kinetic energy are indeed comparable. In this regime, there is an inherent tension between localized and itinerant descriptions of the physics. Moreover, the growing understanding that the nearly-flat bands in MATBG have a topological character[22–24] implies that a simple "atomic" description, in which electrons are localized to individual moiré lattice sites, may not be appropriate. Instead, a picture analogous to that of quantum Hall ferromagnetism has been proposed[25–27]. Understanding this interplay between itineracy and localization, and the new physics that emerges from it, remains a major challenge.

In this work we find that, surprisingly, the correlated state in MATBG above a filling of one electron per moiré site has a hybrid nature, with some of its properties resembling those of an itinerant system, and others which are usually associated with localized electrons. Measurements of the electronic entropy at temperatures of a few Kelvin reveal unusually large excess entropy, which is rapidly suppressed by a moderate in-plane magnetic field. This suggests that even at such low temperatures, there are strongly fluctuating magnetic moments in the system, a behavior typically associated with local

2

moments. On the other hand, our measurements find that this state is metallic without a thermodynamic gap nearby, which is naturally understood within an itinerant picture.

The presence of fluctuating moments at temperatures much below the electronic bandwidth indicates the existence of a new, anomalously small energy scale associated with the bandwidth of magnetic excitations, which is an order of magnitude smaller than the energy scale where a jump appears in the compressibility[21,28]. This jump marks the boundary between the new state at filling factor $\nu > +1$ and the state at lower densities. By tracking the dependence of this boundary on temperature and magnetic field, we find that it exhibits an electronic analogue[29–32] of the famous Pomeranchuk effect[1] in ^{3}He. In that system, a transition from a Fermi liquid to a solid occurs upon increasing temperature, driven by the high nuclear spin entropy of the localized atoms in the solid. Similarly, we find that the new state above $\nu = +1$ is favored relative to the metallic state at $\nu < +1$ upon raising the temperature, due the former's high magnetic entropy. The transition near $\nu = +1$ can also be driven by an in-plane magnetic field, due to the energy gain associated with polarizing the free moments. (A related effect near $\nu = -1$ was proposed very recently, on the basis of transport measurements[33].) The hybrid state observed here, with itinerant electrons coexisting with strongly fluctuating magnetic moments, calls for a new understanding of electron correlations in MATBG.

The data reported here is measured using two independent techniques on two conceptually different devices. The bulk of the results are obtained from local measurements of the electronic entropy[34,35] and compressibility using a scanning nanotube single-electron transistor (SET) on hBN-encapsulated twisted bilayer device (Device 1, Fig. 1a). We focus on a spatial region whose twist angle is close to the theoretical magic angle, and is extremely homogenous over a large area (5µm × 4µm), $\theta = 1.130 \pm 0.005$. Similar results are obtained from global entropy measurements using a monolayer graphene sensor (Device 2, Fig. 3a). Both methods have been described elsewhere[21,36].

The inverse compressibility, $d\mu/dn$, measured in Device 1 at $T = 15$K as a function of the filling factor, $v = n/(n_s/4)$ (where n_s corresponds to four electrons per moiré unit cell), is shown in Fig. 1b. As reported previously[21], sharp jumps in $d\mu/dn$ are observed close to integer v's, reflecting an abrupt reconstruction of the Fermi surface. These were termed Dirac revivals since they were interpreted as resets of partially filled energy bands back to near charge neutrality, leading to the decreased compressibility. The cascade of revivals is already very prominent at this relatively high temperature. Measurements of ρ_{xx} vs. v at various temperatures (Fig. 1c) show insulating behavior at $v = 2,3$ and semi-metallic behavior at $v = 0$. As previously noted[37], ρ_{xx} shows a step-like increase across $v \approx 1$, which gradually disappears decreasing temperature, markedly different than the behavior at other integer $v's$.

The unusual physics near $v = 1$ is revealed from the dependence of $d\mu/dn$ on temperature, T, and parallel magnetic field, $B_{\parallel}$. At low temperature and $B_{\parallel} = 0$T (Fig. 2a), the jump in $d\mu/dn$ occurs at v slightly larger than 1. Increasing the temperature moves the jump towards a lower v, and surprisingly, increases the magnitude of the jump rather than smearing it. Similar measurement with $B_{\parallel} = 12$T at low T (Fig. 2b) exhibits a much larger jump, which is also closer to $v = 1$. With increasing the temperature, the jump remains close to $v = 1$, but oppositely to the $B_{\parallel} = 0$T case, reduces its amplitude and increases its width.

The chemical potential, $\mu(v,T)$ (measured relative to that at charge neutrality), can be obtained by integrating $d\mu/dn$ over density (Fig. 2c,d). Visibly, μ shows a strong temperature dependence for a range of $v's$. This is clearly seen when we plot μ vs. T at two representative $v's$ (Fig. 2c, inset). At $v = 0.2$, μ is practically independent of T (blue). In contrast, at $v = 0.9$ (red) μ is nearly constant until $T \sim 4$K, and then decreases approximately linearly with T. At $v > 1.15$, μ is again nearly temperature independent. Comparing μ at $B_{\parallel} = 0$T (Fig. 2c) and $B_{\parallel} = 12$T (Fig. 2d) reveals a clear contrast: whereas for $B_{\parallel} = 0$T, μ is a decreasing function of temperature for $0.4 < v < 1.15$, for $B_{\parallel} = 12$T, μ decreases with T for $v < 0.9$ and increases for $v > 0.9$.

Measurements of the temperature dependence of μ allow us to directly determine the entropy of the system, by integrating Maxwell's relation: $\left(\frac{\partial s}{\partial \nu}\right)_T = -\left(\frac{\partial \mu}{\partial T}\right)_\nu$, to obtain $s(\nu, T)$ (where s is the entropy per moiré unit cell). For more details on the procedure of extracting the entropy see Supplementary Information section SI1. Fig. 2e shows $s(\nu)$ at $T \approx 10$K (obtained from the slope of μ vs. T in the range $T = 4.5$K $- 15$K), for $B_\parallel = 0$T, 4T, 8T, and 12T. At $B_\parallel = 0$T the entropy is small at low ν's, climbs close to $\nu = 1$, remains roughly constant between $\nu = 1$ and 2 at $s \approx 1.2k_B$, drops rapidly near $\nu = 2$, and decreases towards zero after $\nu = 3$. Clearly, the ν dependence of the entropy is qualitatively different from that of the compressibility: whereas the latter drops sharply near $\nu = 1$ (Fig. 2a), the former remains at a high value.

An important insight into the origin of this large entropy can be gained by examining its magnetic field dependence. As seen in Fig. 2e, the entropy above $\nu = 1$ depends strongly on $B_\parallel$. In particular, at $B_\parallel = 12$T, most of the entropy between $\nu = 1$ and 2 is quenched. The inset shows $s(B_\parallel = 0\text{T}) - s(B_\parallel = 12\text{T})$ vs. ν (the purple shading indicates errorbars; see Supplementary Information SI1). The entropy difference increases sharply near $\nu = 1$, reaching a maximum of $0.85 \pm 0.1k_B$ between $\nu = 1$ and 2. To appreciate the significance of this value, recall that an entropy of $k_B\ln(2) \approx 0.7k_B$ corresponds to two degenerate states on each moiré unit cell. Moreover, in a Fermi liquid, we would expect a much weaker change of the entropy with $B_\parallel$ (Supplementary Information SI4), of the order of k_B times the ratio of the Zeeman energy (about 1meV at $B_\parallel = 12$T) to the bandwidth, estimated to be $W \sim 30$meV (see below). Finally, we observe that at $B_\parallel = 12$T the entropy shows a cascade of drops following each integer ν, similar to the revival drops observed in the compressibility (Supplementary Info. SI5), reproduced by the mean-field calculation (Supplementary Info. SI3). The dramatic quenching of entropy by a moderate in-plane magnetic field is strongly suggestive of its magnetic origin.

To test the robustness of our results, we measured the entropy in a completely different setup, in which a sheet of monolayer graphene senses the chemical potential of MATBG, averaged over the entire device[36] (Fig. 3a). Fig. 3b shows the entropy extracted

in three different temperature ranges. In particular, we see (inset) that the globally measured entropy for $T = 4\text{K} - 16\text{K}$ is in good agreement with the locally measured one over a similar range of temperatures. The agreement is both in the overall shape and magnitude of $s(\nu)$, and in detailed features. The global experiment setup further extends the measurements to higher temperatures. As seen in Fig. 3b, upon raising the temperature, the minimum in the entropy at $\nu = 0$ gradually fills in, evolving from a double-dome structure at low T (corresponding to the valence and conduction flat bands) to a single dome at high T. This dependence is qualitatively reproduced by a naïve calculation for a system of non-interacting electrons, whose density of states rises linearly from the charge neutrality point until the band edges (Fig. 3c). The merging of the domes in $s(\nu)$ occurs when the temperature exceeds a fraction of the bandwidth. Calibrating the bandwidth using the measured entropy at $T \approx 55\text{K}$ gives $W \approx 30\text{meV}$ (where W is the full bandwidth – from valence band bottom to conduction band top, and not only the conduction bandwidth as in ref [21]), in rough agreement with the values deduced from STM[16–19] and compressibility[36] experiments. Of course, we do not expect the free-electron picture to apply at low temperatures, where interactions change the physics dramatically. The measured $s(\nu)$ in the valence band is approximately a mirror image of $s(\nu)$ in the conduction band (Fig. 3b), although it is smaller and with less pronounced features. This is consistent with the weaker $d\mu/dn$ revivals observed in the valence band relative to the conduction band[21,36] (see Supplementary Info. SI9 for comparison of the temperature dependence of $d\mu/dn$).

So far, we have shown that a dramatic change occurs in the entropy and compressibility near $\nu = 1$. The compressibility drops rapidly at the revival transition (Fig. 2a,b), and at approximately the same filling, the magnetic-field-dependent part of the entropy sharply rises (Fig. 2e, inset). This rapid change may be due to a continuous buildup of electronic correlations. Alternatively, it can be interpreted as an underlying first-order phase transition between two distinct phases. Naively, one would then expect a discontinuous jump in thermodynamic properties and hysteretic behavior across the

transition, which are not observed. However, we note that a true first-order phase transition is forbidden in two dimensions in the presence of disorder or long-range Coulomb interactions[38], as these will always broaden the transition into a mesoscale coexistence region (see Supplementary Info. S10). Experimentally, although the revival transition is very sharp and may be consistent with Coulomb- and/or disorder- smeared 1st order transition, we cannot rule out that it is a sharp crossover or a higher order phase transition. Nevertheless, this sharp feature can be tracked precisely to map a phase diagram as the function of temperature and magnetic field. Below, we show that interpreting this revival feature as a proxy for a first-order transition naturally explains much of the underlying physics.

We define the filling factor ν_R of the revival feature as the midpoint of the sharp rise in $d\mu/dn$ (tracking the beginning or the end of the rise leads to similar conclusions, see Supplementary Info. SI5). As we have seen in Fig. 2a, raising the temperature leads to an observable change in ν_R. A similar measurement of $d\mu/dn$ vs. ν at different magnetic fields (Fig. 4a) shows that ν_R also shifts with $B_\parallel$. The measured locations of the revival feature as a function of $B_\parallel$ and T form a surface in the $(\nu, B_\parallel, T)$ space, shown in Fig. 4b. Projections of this surface onto the $(\nu, B_\parallel)$ and (ν, T) planes are presented in Figs. 4c,d. Examining the magnetic field dependence of ν_R (Fig. 4c), we see that at $T = 2.8$K, ν_R is weakly dependent on $B_\parallel$ at low fields, but starts to decrease linearly with field above $B_\parallel \approx$ 4T. A similar crossover is observed at higher temperatures, with a crossover $B_\parallel$ that increases with temperature.

The temperature dependence of ν_R at different magnetic fields (Fig. 4d) highlights another interesting aspect. At $B_\parallel = 0$T (blue) ν_R is linear in T at low temperatures, and curves up at higher temperatures. As $B_\parallel$ increases, the entire curve shifts towards smaller ν's, and simultaneously its slope at low temperatures changes sign. At the highest field, $B_\parallel = 12$T, ν_R first increases with temperature, reaches a maximum at $T \approx 9$K, and then decreases at a higher T.

The phenomenology seen in Figs. 4b-d can be understood in terms of a first-order phase transition at $\nu = \nu_R$ between two phases: a Fermi liquid phase below ν_R, and a 'free moment' phase above it. The latter phase has a high concentration of free moments (about one per moiré site), coexisting with a low density of itinerant electrons. Within this framework, the shift of ν_R as a function of $B_\parallel$ and T reflects the magnetization and entropy differences between the two neighboring phases.

At $B_\parallel = 0\text{T}$, the free moment phase has a higher entropy than the Fermi liquid, due to thermal fluctuations of the moments. Hence, the former phase becomes entropically-favorable at high temperatures. This explains the observed decrease of ν_R with increasing T at low fields (Fig. 4d). Raising the temperature at a fixed ν may therefore drive a transition from the Fermi liquid to the free moments phase, an electronic analogue of the Pomeranchuk effect. As $B_\parallel$ increases and the Zeeman energy exceeds the temperature, the moments become nearly fully polarized and their entropy is quenched (as is observed directly in Fig. 2e). Consequently, at low temperatures and sufficiently high fields, the Fermi liquid phase is favored by raising the temperature. The trend reverses once the temperature exceeds the Zeeman energy. This explains the non-monotonic behavior of ν_R as a function of T, seen at $B_\parallel = 12\text{T}$ in Fig. 4d. The main features of the phase boundary are qualitatively reproduced in an explicit thermodynamic model of the two phases (Supplementary Info. SI7 and insets of Figs. 4b,c,d). While this simple model explains much of the phenomenology, a complete understanding requires a more detailed description of the $\nu < \nu_R$ state (e.g. to account for negative compressibility, revival strength, etc.)[21,36]. Note that the experiment probes moments that couple to in-plane field. This includes Zeeman-coupled spins and may also include the valleys if their in-plane orbital moment is non-zero.

The observation of free magnetic moments at surprisingly low temperatures has profound implications for the physics of MATBG. Low energy magnetic fluctuations are destructive for superconductivity, and their presence may be the limiting factor for the superconducting T_c. Moreover, increased scattering from fluctuating moments can

account for the "strange metal" behavior reported over a broad range of temperatures[39,40].

An important question raised by our observations regards the origin of the free moments. Soft collective modes have been predicted in insulting states of MATBG[25–27], but our experiments show metallic behavior near $v = 1$. Moreover, the energy scale associated with the appearance of free moments is strikingly low (3K or less), much below the microscopic energy scales in the system. Understanding the state near $v = 1$, that combines behaviors associated with electron localization and itineracy, and its surprisingly low onset temperature, poses a key challenge for the theory of MATBG.

References

1.   Pomeranchuk, I. On the thery of He3. *Zh.Eksp.Teor.Fiz* **20**, 919 (1950).

2.   Bistritzer, R. & MacDonald, A. H. Moiré bands in twisted double-layer graphene. *Proc. Natl. Acad. Sci.* **108**, 12233–12237 (2011).

3.   Cao, Y. *et al.* Correlated insulator behaviour at half-filling in magic-angle graphene superlattices. *Nature* **556**, 80–84 (2018).

4.   Cao, Y. *et al.* Unconventional superconductivity in magic-angle graphene superlattices. *Nature* **556**, 43–50 (2018).

5.   Li, G. *et al.* Observation of Van Hove singularities in twisted graphene layers. *Nat. Phys.* **6**, 109–113 (2010).

6.   Suárez Morell, E., Correa, J. D., Vargas, P., Pacheco, M. & Barticevic, Z. Flat bands in slightly twisted bilayer graphene: Tight-binding calculations. *Phys. Rev. B* **82**, 121407 (2010).

7.   Regan, E. C. *et al.* Mott and generalized Wigner crystal states in WSe2/WS2 moiré superlattices. *Nature* **579**, 359–363 (2020).

8.   Tang, Y. *et al.* Simulation of Hubbard model physics in WSe2/WS2 moiré superlattices. *Nature* **579**, 353–358 (2020).

9.   Yankowitz, M. *et al.* Tuning superconductivity in twisted bilayer graphene. *Science* **363**, 1059–1064 (2019).

10.   Lu, X. *et al.* Superconductors, orbital magnets and correlated states in magic-angle bilayer graphene. *Nature* **574**, 653–657 (2019).

11.   Nuckolls, K. P. *et al.* Strongly Correlated Chern Insulators in Magic-Angle Twisted Bilayer Graphene. *arXiv* 2007.03810 (2020).

12.   Wu, S., Zhang, Z., Watanabe, K., Taniguchi, T. & Andrei, E. Y. Chern Insulators and Topological Flat-bands in Magic-angle Twisted Bilayer Graphene. *ArXiv* 2007.03725 (2020).

13.   Das, I. *et al.* Symmetry broken Chern insulators and magic series of Rashba-like

Landau level crossings in magic angle bilayer graphene. *Arxiv* 2007.13390 (2020).

14. Sharpe, A. L. *et al.* Emergent ferromagnetism near three-quarters filling in twisted bilayer graphene. *Science* **365**, 605–608 (2019).

15. Serlin, M. *et al.* Intrinsic quantized anomalous Hall effect in a moiré heterostructure. *Science* **367**, 900–903 (2020).

16. Kerelsky, A. *et al.* Maximized electron interactions at the magic angle in twisted bilayer graphene. *Nature* **572**, 95–100 (2019).

17. Xie, Y. *et al.* Spectroscopic signatures of many-body correlations in magic-angle twisted bilayer graphene. *Nature* **572**, 101–105 (2019).

18. Jiang, Y. *et al.* Charge order and broken rotational symmetry in magic-angle twisted bilayer graphene. *Nature* **573**, 91–95 (2019).

19. Choi, Y. *et al.* Electronic correlations in twisted bilayer graphene near the magic angle. *Nat. Phys.* **15**, 1174–1180 (2019).

20. Tomarken, S. L. *et al.* Electronic Compressibility of Magic-Angle Graphene Superlattices. *Phys. Rev. Lett.* **123**, 046601 (2019).

21. Zondiner, U. *et al.* Cascade of phase transitions and Dirac revivals in magic-angle graphene. *Nature* **582**, 203–208 (2020).

22. Po, H. C., Zou, L., Vishwanath, A. & Senthil, T. Origin of Mott insulating behavior and superconductivity in twisted bilayer graphene. *Phys. Rev. X* **8**, 031089 (2018).

23. Song, Z. *et al.* All Magic Angles in Twisted Bilayer Graphene are Topological. *Phys. Rev. Lett.* **123**, 036401 (2019).

24. Ahn, J., Park, S. & Yang, B.-J. Failure of Nielsen-Ninomiya Theorem and Fragile Topology in Two-Dimensional Systems with Space-Time Inversion Symmetry: Application to Twisted Bilayer Graphene at Magic Angle. *Phys. Rev. X* **9**, 021013 (2019).

25. Bultinck, N. *et al.* Ground State and Hidden Symmetry of Magic-Angle Graphene at Even Integer Filling. *Phys. Rev. X* **10**, 031034 (2020).

26. MacDonald, A. H. private communication.

27. Wu, F. & Das Sarma, S. Collective Excitations of Quantum Anomalous Hall Ferromagnets in Twisted Bilayer Graphene. *Phys. Rev. Lett.* **124**, 046403 (2020).

28. Wong, D. *et al.* Cascade of electronic transitions in magic-angle twisted bilayer graphene. *Nature* **582**, 198–202 (2020).

29. McWhan, D. B. *et al.* Electronic Specific Heat of Metallic Ti-Doped V2O3. *Phys. Rev. Lett.* **27**, 941–943 (1971).

30. Spivak, B. & Kivelson, S. A. Phases intermediate between a two-dimensional electron liquid and Wigner crystal. *Phys. Rev. B* **70**, 155114 (2004).

31. Continentino, M. A., Ferreira, A. S., Pagliuso, P. G., Rettori, C. & Sarrao, J. L. Solid state Pomeranchuk effect. *Phys. B Condens. Matter* **359**–**361**, 744–746 (2005).

32. Pustogow, A. *et al.* Quantum spin liquids unveil the genuine Mott state. *Nat. Mater.* **17**, 773–777 (2018).

33. Saito, Y. *et al.* Isospin Pomeranchuk effect and the entropy of collective excitations in twisted bilayer graphene. *ArXiv* 2008.10830 (2020).

34. Kuntsevich, A. Y., Tupikov, Y. V, Pudalov, V. M. & Burmistrov, I. S. Strongly correlated two-dimensional plasma explored from entropy measurements. *Nat. Commun.* **6**, 7298 (2015).

35. Hartman, N. *et al.* Direct entropy measurement in a mesoscopic quantum system. *Nat. Phys.* **14**, 1083–1086 (2018).

36. Park, J. M., Cao, Y., Watanabe, K., Taniguchi, T. & Jarillo-Herrero, P. Flavour Hund's Coupling, Correlated Chern Gaps, and Diffusivity in Moir'e Flat Bands. *Arxiv* 2008.12296 (2020).

37. Chen, S. *et al.* Electrically tunable correlated and topological states in twisted monolayer-bilayer graphene. *Arxiv* 2004.11340 (2020).

38. Spivak, B. & Kivelson, S. A. Transport in two dimensional electronic micro-emulsions. *Ann. Phys.* **321**, 2071–2115 (2006).

39. Cao, Y. *et al.* Strange Metal in Magic-Angle Graphene with near Planckian Dissipation. *Phys. Rev. Lett.* **124**, 076801 (2020).

40. Polshyn, H. *et al.* Large linear-in-temperature resistivity in twisted bilayer graphene. *Nat. Phys.* **15**, 1011–1016 (2019).

41. Uri, A. *et al.* Mapping the twist-angle disorder and Landau levels in magic-angle graphene. *Nature* **581**, 47–52 (2020).
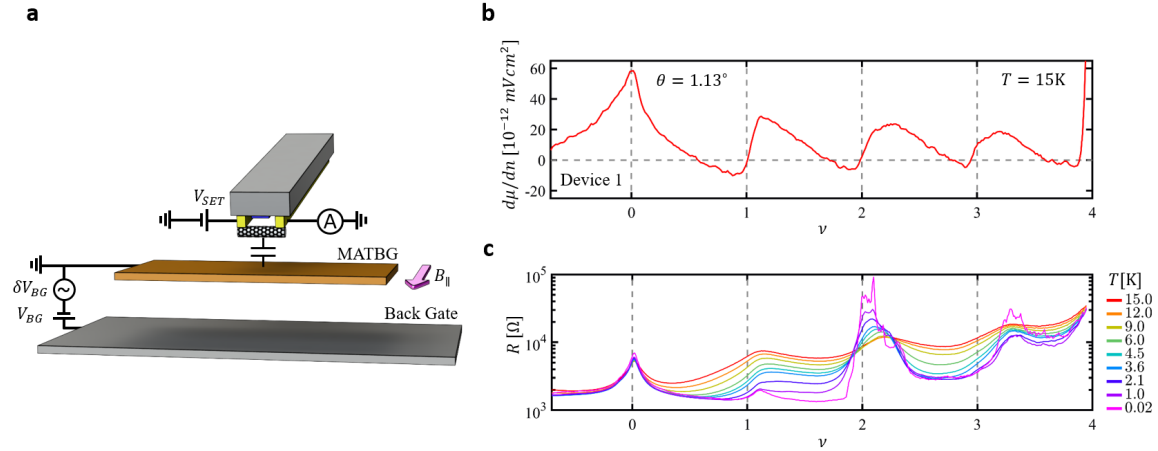
Figure 1: Experimental setup and device characterization. a. A nanotube-based single electron transistor (SET) is used to measure the local electronic compressibility and entropy of magic angle twisted bilayer graphene (MATBG). The MATBG is encapsulated between top and bottom h-BN layers (not shown) and has a metallic back-gate. By monitoring the current through the SET, we track changes in the MATBG chemical potential, $d\mu$, in response to a density modulation, dn, produced by an a.c. voltage on the back-gate[21], δV_{BG}. A d.c. back-gate voltage, V_{BG}, sets the overall carrier density in the MATBG, n. Some of the measurements are performed in a parallel magnetic field, $B_{\parallel}$ (indicated). **b.** Inverse compressibility, $d\mu/dn$, measured as a function of the moiré lattice filling factor, $\nu = n/(n_s/4)$, at $T = 15K$ (n_s is the density that correspond to 4 electrons per moiré site). Measurements are done on a large spatial domain ($\sim 5\mu m \times 4\mu m$) throughout which the twist angle is extremely homogenous, $\theta = 1.130° \pm 0.005$ (measured by spatial mapping of the V_{BG} that corresponds to n_s, as in Refs. [21,41]). As seen previously[21], a jump of $d\mu/dn$ appears near all integer filling factors. This jump corresponds to a Fermi surface reconstruction, in which some combination of the spin/valley flavors filling is reset back to near the charge neutrality point, and correspondingly $d\mu/dn$ shows a cascade of sawtooth features as a function of density. The trace is measured at $T = 15K$, showing that even at this high temperature this sawtooth cascade is well developed **c.** Two-probe resistance, R, measured as a function of ν and temperature. Notice that unlike the inverse compressibility, which measures a local quantity, the resistance gives an averaged result over domains with different twist angle. Therefore, the resistance maxima are slightly shifted from the usual integer ν values, probably because another domain with a small difference in twist angle dominates the transport characteristics globally.
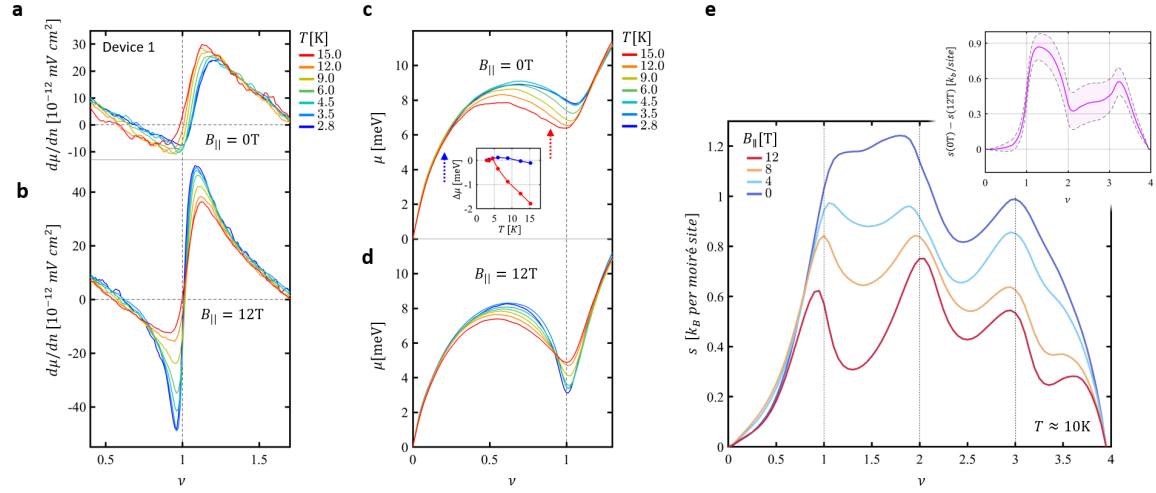
Figure 2: Measurement of large magnetic entropy above $\nu = 1$. a. Inverse compressibility, $d\mu/dn$, as a function of ν, near $\nu = 1$, measured at zero parallel magnetic field, $B_\parallel = 0T$, and at several temperatures. With increasing T, the jump in $d\mu/dn$ moves toward lower ν and becomes stronger. **b.** Same measurement done at $B_\parallel \approx 12T$. Here, opposite to the zero-field case, increasing T reduces the magnitude of the $d\mu/dn$ jump, as expected from thermal smearing. **c.** The chemical potential $\mu(\nu)$ (relative to that of the charge neutrality point) at $B_\parallel = 0T$, obtained by integrating the $d\mu/dn$ signal in panel a with respect to n. Inset: $\mu(T, \nu) - \mu(T = 2.8K, \nu)$ for $\nu = 0.2$ (blue) and $\nu = 0.9$ (red). At $\nu = 0.2$ the chemical potential is nearly temperature independent, whereas at $\nu = 0.9$ it is roughly constant until $T \sim 4K$ and then start decreasing approximately linearly with T. **d.** Similar to c, but at $B_\parallel = 12T$. In contrast to the zero-field case, here, below $\nu \approx 0.9$, μ decreases with T while above $\nu \approx 0.9$ μ increases with T. **e.** The electronic entropy in units of k_B per moiré unit cell, as a function of ν at $T \approx 10K$ and at various parallel magnetic fields, $B_\parallel = 0,4,8,12T$. To obtain the entropy we determine the partial derivative $(\partial\mu/\partial T)_{\nu,B_\parallel}$ from a linear fit to the measured μ vs. T in the range $T = 4.5K - 15K$. The entropy per moiré cell is then obtained by integrating Maxwell's relation: $(\partial s/\partial\nu)_{T,B_\parallel} = -(\partial\mu/\partial T)_{\nu,B_\parallel}$, over ν (see Supp Info. for details). At $B_\parallel = 0$ the entropy climbs rapidly near $\nu = 1$ to a value of $1.2k_B$ per moiré cell. Inset: the difference between the entropies at low and high fields, $s(B_\parallel = 0T) - s(B_\parallel = 12T)$. The purple shading shows the estimated error bar.
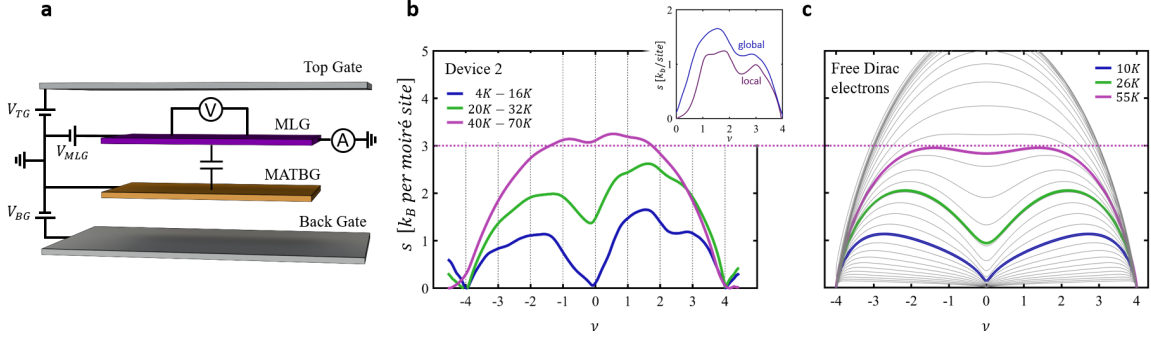
16

Figure 3: Temperature dependence of the Entropy. a. Experimental setup for measuring the global entropy, averaged over the entire device[36]. The device consists of MATBG and a monolayer graphene (MLG) sensor layer, separated by an ultrathin ($1\ nm$) layer of h-BN (not shown), as well as top and bottom metallic gates. By balancing the electrochemical potential of the adjacent layers in the device, we can obtain the relationship between the density and chemical potential of MATBG and MLG and the gate voltages applied to the system. In the special case where the density of MLG is zero, i.e. at its charge neutrality point, the chemical potential of MATBG is directly proportional to the voltage applied to the top gate. This technique allows us to reliably extract the chemical potential and entropy of MATBG at temperatures up to 70 K. **b.** The measured entropy, in units of k_B per moiré unit cell, as a function of ν at three different temperature ranges (top legend). The entropy derivative, $ds/d\nu$, is obtained from a linear fit to μ vs. T in the corresponding temperature range, and is then integrated over ν to yield the entropy per moiré unit cell (similar to Fig. 2e). Inset: comparison between the ν dependences of the entropies, measured at the low temperature range, obtained from local and global measurements. **c.** The entropy as a function of ν and T calculated for a system of four degenerate non-interacting Dirac bands (whose density of states climbs linearly with energy from the Dirac point to the end of the conduction or the valence band). The color-coded lines show the curves whose temperatures correspond to the mean of the temperature ranges of the experimental curves. The gray lines represent the entire evolution from zero temperature to high temperature, where the entropy saturates on a value of $8ln(2) \approx 5.5$, where the factor 8 reflects the total number of energy bands. A bandwidth of $W = 30meV$ is chosen such that the calculated value of the entropy at the highest temperature roughly matches the one obtained from the measured curve at the same temperature.

Figure 4: Experimental phase diagram. a. The inverse compressibility, $d\mu/dn$, measured as a function of ν near $\nu = 1$, at several values of parallel magnetic field, $B_\parallel$. We track the filling factor that corresponds to the center the jump in $d\mu/dn$ (labeled ν_R). Visibly, the application of $B_\parallel$ pushes ν_R to lower values. **b.** Measured ν_R as a function of $B_\parallel$ and T, plotted as dots in the $(\nu, B_\parallel, T)$ space (the dots are colored by their temperature). The dashed lines are polynomial fits to the dots at constant $B_\parallel$ or constant T. Inset: the same surface calculated from a simple model that assumes a transition between a low T Fermi liquid and a high T metallic phase that contains one free moments per moiré site (see text). **c.** Projection of the data in panel b onto the $(\nu, B_\parallel)$ plane, showing the dependence of ν_R on $B_\parallel$ for various temperatures. At low fields, ν_R is independent of field but it becomes linear in $B_\parallel$ at high fields, a behavior expected from the field polarization of free moments (see text). Inset: curves calculated from the model. **d.** Projection onto the (ν, T) plane, showing the dependence of ν_R on T for various magnetic fields. At $B_\parallel = 0T$, ν_R is linear in T at small T 's and then curves up at higher T's. At high magnetic field, the dependence of ν_R on T becomes non-monotonic. Inset: curves calculated from the model.